A CELL BOUNDARY ELEMENT METHOD APPLIED TO LAMINAR VORTEX-SHEDDING FROM ARRAYS OF CYLINDERS IN VARIOUS ARRANGEMENTS

T. Farrant[†]

Computational Engineering and Design Centre, Highfield
Southampton SO17 1BJ, U.K.

AND

M. Tan AND W. G. Price

School of Engineering Sciences, Ship Science, University of Southampton
Highfield, Southampton SO17 1BJ, U.K.

A cell boundary element method is used to solve the two-dimensional incompressible Navier–Stokes equation for vortex-shedding flows around arrays of cylinders. The method is a hybrid scheme using a boundary element method in each fluid cell discretization with a finite element procedure to solve for the global fluid problem. Computations are presented of two-dimensional flow characteristics and interactive forces associated with flows around four equispaced cylinders of equal diameter, and two cylinders, one with circular cross-section and the other elliptical. It was found that behaviour such as in-phase vortex-shedding, anti-phase vortex shedding and synchronized vortex shedding, which are well-known characteristics for flows past arrangements of two circular cylinders, were also present in these more complicated flows. The application of the cell boundary element method to these flow problems, using an unstructured fluid domain mesh idealization, proved straightforward and required no modification for variation of the number of bodies or their shape.   © 2000 Academic Press

1. INTRODUCTION

In the design of deepwater floating oil production systems, there is a need to analyse the hydrodynamic behaviour of key parts of the structure such as the risers for production, export and injection of gas or water. Typically, these offshore production platforms are in the form of ship-shaped floating production, storage and off-loading facilities (FPSO), tension leg platforms (TLP) or spars [see, for example, Hatton (1999)].

In oilfield developments now exceeding 1000 m water depth, the cross-section of the flexible riser may be typically less than 2 m and can experience ocean currents with velocities in excess of 1·0 m/s. The latter are sufficient to provide the necessary energy for self-excited vibration of the structure due to vortex shedding. This is often known as vortex-induced vibration (VIV) and is a major cause of fatigue damage to welds in risers.

Accurate fatigue life prediction relies, in part, on the accuracy of the model used to represent the fluid action on the structure. Nevertheless, even in multi-cylinder arrangements, most fluid–structure interaction studies are limited to the case of a single cylinder. In contrast, this paper investigates vortex-shedding flows around pipe bundle geometries, with

---

[†]Now at 2H Offshore Ltd, Woking, U.K.

the aim of identifying differences between single cylinder flows and those around multiple cylinders. Of particular importance for fatigue life prediction is the frequency and magnitude of the vibration. Knowledge of these properties is required when using material fatigue strength design curves in the form of S–N curves, where S is the cyclic stress magnitude and N is the number of cycles to failure [see, for example, Barltrop & Adams (1991) and Gran (1992)].

In most cases, the Reynolds number is large and the flows are transitional or turbulent. Because of this, many of the flow features are three-dimensional and of a complex structural nature. These characteristics make analysis difficult, even using direct numerical simulation of the governing Navier–Stokes equations; see, for example, Hunt (1995) and Gatski et al. (1996). In the absence of the ability to solve these fluid problems directly, a number of approaches have evolved to predict the behaviour of such systems, at least in some restricted cases. For example, it is the practice to assume that the flow can be treated as two-dimensional, even if the bluff body is not perpendicular to the uniform stream, by resolving the flow normal to the body surface and assuming this to be the characteristic velocity over the body (Blevins 1990). Furthermore, the fluid action is often modelled empirically by a simple sinusoidal excitation or by a more complicated wake oscillator model [see, for example, Hassan (1962), Bishop & Hassan (1964) and Sarpkaya & Isaacson (1981)]. While such approaches are of great utility, the assumptions involved in development (i.e. the two-dimensional nature of the flow, and the isolation of the cylinder, etc.) restrict their applicability. In fact, it is common practice in industry to apply a safety factor of 100 to predicted fatigue life results when using such approaches.

Direct numerical solution of the Navier–Stokes equations governing the fluid motion, can be used to represent more accurately the vortex dynamics of the flow. However, evaluating the fluid action is computationally intensive because all the details of the wake and the boundary layer must be resolved [see, for example, Gatski et al. (1996)]. At present it is not possible to compute such flows unless the Reynolds number is moderately low (Re < 10 000) or a sub-grid scale turbulence model is used [see, for example Cheng & Armfield (1994)]. In spite of this, it is observed in the experiment (Williamson 1985; Zdravkovich 1977) that many of the large-scale characteristics of transitional or turbulent flows show a resemblance to those at much lower Reynolds number. For this reason, numerous numerical studies have been performed at these lower Reynolds numbers; see, for example, Van de Vosse et al. (1986), Slaouti & Stansby (1994), Persillon et al. (1995) and Zhang & Zhang (1997).

In the case where there are multiple bodies in close proximity, computation of the flow becomes even more problematical, due to the need to model additional body surfaces and to include large areas of fluid domain between and around the cylinders. Perhaps because of this, investigations have concentrated on flows around two cylinders in various arrangements (i.e. side by side, tandem, or staggered) and at Reynolds numbers Re ≤ 1000. Examples of such investigations are described by Chang & Song (1990), Tezduyar et al. (1990), Li et al. (1991), Johnson et al. (1993), Slaouti & Stansby (1992) and Mittal et al. (1997).

The present study focuses on two-dimensional, laminar vortex shedding from multiple-cylinder configurations. The examples chosen are idealizations of cylinder arrangements found in offshore engineering, i.e. tubular structures, risers, etc. Therefore, the cases investigated involve isolated cylinders, two cylinders with circular or elliptical cross-sections side by side or in tandem in the flow, and four cylinders of equal diameter and at equal spacings in various flows. To achieve descriptions of the interactive vortex shedding, the mathematical model developed needs to combine the ability to idealize arbitrary-shaped structures and a large fluid domain with such detail to characterize accurately in

space and time the interacting phenomena. Tan *et al.* (1999) developed a cell boundary element method (cell BEM) to solve viscous fluid–structure interaction problems modelled by the Navier–Stokes equations. A hybrid approach was proposed incorporating boundary element and finite element methods. That is, cell equations are generated using the principles of the boundary element method, with global equations derived following the procedures of the finite element method. A primitive-variable formulation with an unstructured mesh representation of the fluid forms the basis of the hybrid approach which can be applied to both two- and three-dimensional problems. The validation of the developed numerical scheme under study, involving analytical and numerical procedures, was undertaken by Farrant (1999), Tan *et al.* (1999) and Farrant *et al.* (1999) using a wide selection of well-documented flow solutions, i.e. Couette flows, backward-facing step flows, driven cavity flows, and flows past circular cylinders, etc. They demonstrated the accuracy and robustness of the method through detailed comparisons with theoretical and experimental findings. The present investigation extends the application of the cell boundary element method to arrays of cylinders arbitrarily positioned in the fluid flow. Since the approach and numerical scheme of the study are documented elsewhere, a brief résumé of the mathematical model is included herein.

2. MATHEMATICAL THEORY

The boundary element method described by Price & Tan (1992) treats the nonlinear convective term of the Navier–Stokes equations as a *pseudo-body force*. This approach required a solution process involving full matrices and had a negative impact on the overall efficiency and stability of the numerical scheme (Tan 1994). To overcome these difficulties, Tosaka & Kakuda (1988) developed a generalized boundary element method to tackle nonlinear problems.

This generalized method was used as the basis of an approach by Tan *et al.* (1999) to solve incompressible Navier–Stokes flow problems. In effect, this approach is a hybrid scheme based on the boundary element and finite element methods. That is, instead of introducing the integral equation to the whole fluid–structure system directly, the fluid domain is divided into a large number of cells or elements, in a similar discretization process to the finite element or finite volume methods. The boundary element method is then applied to each cell to generate sets of algebraic equations which consistently represent the Navier–Stokes equations on each cell. Application of continuity conditions, on fluid velocity and surface traction force, at the cell interfaces allows a global system of algebraic equations to be obtained and solved. This global system describes the dynamics of the fluid in the whole domain.

To apply the boundary element method on a cell in time-dependent problems, the nonlinear term in the Navier–Stokes equations which models the fluid in each cell is resolved at each time step. The nonlinear nature of the equation is modelled through a suitably time-stepping scheme.

The fundamental solution needed for the cell calculation is a modified Oseen solution which has been derived by Price & Tan (1992) for two- and three-dimensional problems. The convective velocity involved in the Oseen solution changes not only during time stepping but also spatially from cell to cell. This procedure improves numerical stability, since the nonlinear feature of the flow is represented in the fundamental solution.

The cell BEM is a primitive-variable formulation which allows easy application to three-dimensional problems. Furthermore, the use of the velocity and surface traction force as the basic unknowns provides a convenient way of expressing boundary conditions.

In this paper the formulation is described briefly with particular emphasis on its use with two-dimensional, time-dependent problems. For a complete description of the method for steady-state and time-dependent problems with validation examples, see Tan *et al.* (1999).

2.1 GOVERNING EQUATIONS AND INTEGRAL EQUATION

Figure 1 illustrates a fluid domain represented by an unstructured cell idealization, with individual cell domain Ω and surface Σ. Assuming the fluid incompressible, the Navier–Stokes equation and continuity equation describing the nondimensional fluid flow velocity, $v(x, t)$, and nondimensional pressure, $p(x, t)$, are given respectively by

$$\dot{v}_j + (v_j v_k)_{,k} + p_{,j} - [v_e(v_{j,k} + v_{k,j})]_{,k} = 0 , \tag{1}$$

$$v_{j,j} = 0 . \tag{2}$$

Equations (1) and (2) are in nondimensional form after applying a change of variable. Namely,

$$x_j = \frac{x_j'}{L'}, t = \frac{U'}{L'} t', v_j = \frac{v_j'}{U'}, \ p = \frac{p'}{\rho' U'^2},$$

where a prime denotes a dimensional quantity. Here L' and U' are the characteristic length and velocity, respectively. For bluff bodies in a uniform stream flow, normally the characteristic length is taken as the largest body dimension across the stream and the characteristic velocity is that of the stream. Therefore, in equation (1), $v_e = 1/\text{Re}$ and Reynolds number $\text{Re} = \rho' U' L'/\mu'$, where density and viscosity are denoted by ρ' and μ' respectively, and a tensor index notation with summation convention is adopted to retain compact mathematical expressions. An example of this notation is given by the convective term

$$(v_j v_k)_{,k} = \sum_{k=1} \frac{\partial(v_j v_k)}{\partial x_k},$$

where the upper limit of the summation takes the value of 2 or 3 for two- and three-dimensional problems, respectively.

Before formation of an integral equation involving the Navier–Stokes equations, it is beneficial both analytically and for enhanced computational efficiency to introduce a scheme to resolve the nonlinear convective term in equation (1). For time-dependent problems this can be achieved by using a differencing approximation which maintains an accuracy of second order, Δt^2, in the $(n + 1)$th time step. For this scheme, contributions from the velocity field at the nth and $(n - 1)$th time steps are also included. That is,

$$h_j + (v_j \tilde{v}_k)_{,k} + p_{,j} - [v_e(v_{j,k} + v_{k,j})]_{,k} = 0, \tag{3}$$

where

$$h_j = \frac{1}{2\Delta t} [3v_j - 4v_j^{(n)} + v_j^{(n-1)}]$$

and

$$\tilde{v}_k = 2v_k^{(n)} - v_k^{(n-1)}.$$

Regardless of the time-marching scheme employed it is possible to form an integral equation using the modified form of the Navier–Stokes equations, equation (3). Integrating over the cell domain Ω, while incorporating two arbitrary weighting functions v_{sj}^* and p_s^*,

and applying Gauss's theorem leads to the following integral equation (Tan 1994):

$$\int_\Omega \{v_{sj}^*[h_j + (v_j\tilde{v}_k)_{,k} + p_{,j} - (v_e(v_{j,k} + v_{k,j}))_{,k}] + p_s^* v_{j,j}\}\, \mathrm{d}\Omega$$

$$+ \int_\Omega \{v_j[\tilde{v}_k v_{sj,k}^* + p_{s,j}^* + (v_e(v_{sj,k}^* + v_{sk,j}^*))_{,k}] + pv_{sj,j}^*\}\, \mathrm{d}\Omega$$

$$= \int_\Sigma [v_j(\tilde{v}_k n_k v_{sj}^* + R_{sj}^*) - R_j v_{sj}^*]\,\mathrm{d}\Sigma + \int_\Omega h_j v_{sj}^*\,\mathrm{d}\Omega, \tag{4}$$

where n denotes the outward normal to the surface Σ. Furthermore, $R_j = -pn_j + v_e(v_{j,k} + v_{k,j})\,n_k$ represents the jth component of the dimensionless traction force on the boundary surface. The variable R_{sj}^* is defined as

$$R_{sj}^* = p_s^* n_j + v_e(v_{sj,k}^* + v_{sk,j}^*)n_k\,.$$

The integral equation (4) is valid for any functions v_j, p, v_{sj}^* and p_s^*, provided that all terms involved are integrable. Since the weighting functions v_{sj}^* and p_s^* are arbitrary, it is possible to choose them in such a way as to satisfy the equations

$$\tilde{v}_k v_{sj,k}^* + p_{s,j}^* + (v_e(v_{sj,k}^* + v_{sk,j}^*))_{,k} = -\delta_{sj}\Delta(x - \xi), \tag{5}$$

$$v_{sj,j}^* = 0, \tag{6}$$

where δ and Δ are Kronecker and Dirac delta functions, respectively. The solution of equations (5) and (6) is referred to as the fundamental solution and represents the response of the system to a point excitation. Choosing the functions to satisfy equations (5) and (6), according to the boundary element method, considerably simplifies equation (4) to

$$C(\xi)v_s(\xi, t) + \int_\Sigma v_j(\tilde{v}\cdot nv_{sj}^* + R_{sj}^*)\,\mathrm{d}\Sigma = \int_\Sigma R_j v_{sj}^*\,\mathrm{d}\Sigma - \int_\Omega h_j v_{sj}^*\,\mathrm{d}\Omega, \tag{7}$$

where

$$C(\xi) = \begin{cases} 0 & \text{if } \xi \notin (\Omega \cup \Sigma), \\ \frac{1}{2} & \text{if } \xi \in \Sigma, \\ 1 & \text{if } \xi \in \Omega. \end{cases} \tag{8}$$

In equation (7) the velocity everywhere in the cell is expressed as surface integrals of velocity v and traction R on the cell boundary, as well as a domain integral which can also be calculated from the values of velocity on the boundary. Therefore, equation (7) represents a relationship between the cell velocity field and the surface traction force.

A description of the derivation process for the fundamental solution is given by Tan *et al.* (1999) and further details are discussed by Price & Tan (1990). This description will not be repeated here. However, it should be noted that to simplify the process of solution of equations (5) and (6), a further approximation is introduced to replace the unknown convective velocity $\tilde{v}_k$ by a cell average velocity u_k. This was shown by Tan *et al.* (1999) to have an insignificant effect on overall solutions after the completion of a large number of numerical tests.

2.2. NUMERICAL MODELLING AND THE CELL EQUATIONS

To solve a fluid flow problem, the domain is discretized into a large number of cells in the unstructured form as shown in Figure 1. For each cell, it is possible to approximate the integral equation (7) through adoption of assumed distributions of the unknowns v and
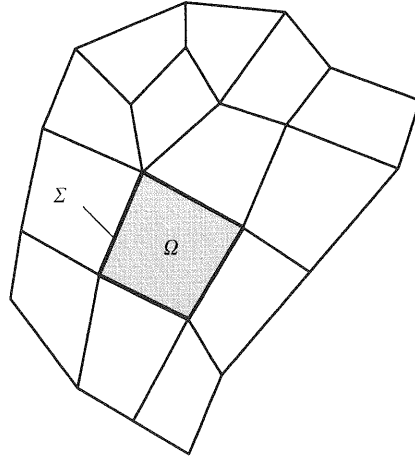
Figure 1. A cell within the global fluid domain idealized by an unstructured mesh.

R based on their values at collocation points on the cell boundary. This procedure is developed from the standard boundary element discretization methods; see, for example, Brebbia (1978) and Brebbia & Walker (1980a, b). The introduction of this approximation procedure allows a set of algebraic equations to be obtained from the integral equation (7). To illustrate this process, a discussion follows for the two-dimensional, time-dependent case in which a second-order time-stepping scheme is used, and cells are restricted to quadrilateral shapes with collocation points at the centre of each edge.

A typical cell is shown in Figure 2. The collocation points and edges are assigned a common local numbering system as there is only one control point per edge. Applying this cell structure to the integral equation (7) results in the following approximate form:

$$C(\xi) v_s(\xi, t) + \sum_{l=1}^{l=4} \int_{(l)} (\boldsymbol{u} \cdot \boldsymbol{n} v_{sj}^* + R_{sj}^*) \sum_{i=1}^{i=4} N_v^{(i)} v_j^{(i)} \, d\Sigma$$

$$- \frac{1}{\Delta t} \int_\Omega \sum_{i=1}^{i=4} N_v^{(i)} v_j^{(i)} v_{sj}^* \, d\Omega$$

$$= \sum_{l=1}^{l=4} \int_{(l)} v_{sj}^* \sum_{i=1}^{i=4} N_r^{(i)} R_j^{(i)} \, d\Sigma$$

$$+ \frac{1}{\Delta t} \int_\Omega \sum_{i=1}^{i=4} N_a^{(i)} H(v_j^{(n)}, v_j^{(n-1)}) v_{sj}^* \, d\Omega. \tag{9}$$

Here, $N_v^{(i)}$, $N_r^{(i)}$ and $N_a^{(i)}$ are sets of interpolation polynomials for the velocity field v_j, the surface traction force R_j and the velocity from the previous time step $v^{(n)}$, respectively. The subscript a is used, because the last integral describes the acceleration term in the Navier–Stokes equations. The function $H(v_j^{(n)}, v_j^{(n-1)})$ is due to the second-order time-differencing scheme and its value is determined by velocity values from the previous nth and $(n-1)$th time steps. The index $l = 1, 2, 3, 4$ indicates a line integration along each edge of the cell. However, the index i, also varies from 1 to 4 but moves through the collocation points and the corresponding interpolation functions as required by the integration. For
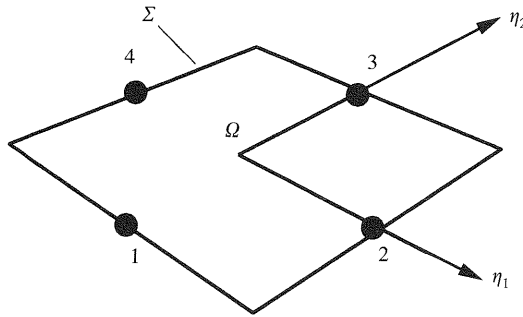
Figure 2. The two-dimensional quadrilateral cell definition.

a more detailed description of the interpolation functions and the integration of the fundamental solution, see Tan *et al.* (1999).

When ξ in equation (9) moves to the coordinates of each collocation point in turn and the index s is allowed to take the values 1 and 2 (because of two dimensions), eight simultaneous algebraic equations are generated for the cell. Therefore, if the superscript e denotes the eth cell, the eight algebraic equations can be expressed in the form

$$A_v^{(e)} V^{(e)} = A_r^{(e)} R^{(e)} + b^{(e)}.$$

Here, $V^{(e)}$ and $R^{(e)}$ are column arrays of the velocity field and surface traction force components at the collocation points. The 8×8 matrix $A_v^{(e)}$ groups coefficients which arise due to the evaluation of the two integrals on the left-hand side of equation (9) involving the velocity at the collocation points. The 8×8 matrix $A_r^{(e)}$ includes coefficients from the boundary integral on the right-hand side of equation (9) relating to the values of the surface traction force at the collocation points. The single column array $b^{(e)}$ contains entries evaluated from the domain integral incorporating the contribution of the velocity from the last time step, $v_j^{(n)}$.

In order to construct a global system of equations to solve for the velocity field, using the eight cell equations, an expression for $R^{(e)}$ is obtained in the form

$$R^{(e)} = C^{(e)} V^{(e)} - d^{(e)}, \tag{10}$$

where $C^{(e)}$ and $d^{(e)}$ are solutions of the equations

$$A_r^{(e)} C^{(e)} = A_v^{(e)}, \quad A_r^{(e)} d^{(e)} = b^{(e)}. \tag{11}$$

Algebraic cell equations, as defined by (10), can be obtained for every cell in the mesh. A combination of the equation sets from all the cells allows solution of the global fluid problem.

2.3. THE GLOBAL EQUATIONS

To solve the global fluid problem, the cell equations are assembled into a global system using cell interface conditions applied at the collocation points. For the surface traction force R, the forces must be equal and opposite to one another on common collocation points between neighbouring cells. Additionally, the velocity v must be equal at common collocation points. Mathematically, this can be expressed as

$$R^{(i)} + R'^{(i')} = 0 \text{ and } v^{(i)} = v'^{(i')}, \tag{12}$$

where $R^{(i)}$, $R'^{(i')}$, $v^{(i)}$ and $v'^{(i')}$ are the values of the traction and velocity on the same collocation point belonging to different cells.

The global system of equations is assembled according to a global order which is defined using a consecutive numbering system for the collocation points in the mesh. This numbering process is identical to that used in the construction of the stiffness matrix described in finite element analysis of structures [see, for example, Cook *et al.* (1989)]. Using the inter-cell conditions, the global numbering system and the cell equation sets generated by equation (9), a global system of algebraic equations describing the velocities at the collocation points is created. That is,

$$DV = F, \tag{13}$$

where V is the array of velocity values on the collocation points in the global order, D is constructed from the coefficients in $C^{(e)}$ [see equation (10)], and F represents the contributions from $b^{(e)}$. When velocities are specified at the domain boundary, for example with the no-slip condition on a body surface, the equations are rearranged so that for the specified boundary collocation points the unknown degree of freedom becomes the traction force R. A detailed description of the implementation of boundary conditions can be found in Tan *et al.* (1999).

Each cell only interacts directly with its neighbours through shared collocation points. This feature of the scheme leads to the global equation system matrix D being symmetrical in form although the values of its nonzero entries are not. For such matrices, the skyline method of matrix storage is efficient (Bathe & Wilson 1976).

3. SIMPLE FLOW CONFIGURATIONS AND VALIDATION

An extensive validation of the cell BEM was performed by Tan *et al.* (1999) for standard analytical and experimental benchmarks, such as Couette channel flow, driven cavity flow, and flow over a backward-facing step. This validation was extended by Farrant *et al.* (1999) to vortex-shedding flows around circular cylinders in isolation or in pairs.

The current study investigates flows around cylinder combinations, some with different cross-sectional shape. These examples represent significant departures from the simple cases undertaken previously by the authors and emphasize the necessity of unstructured fluid domain idealizations. To aid interpretation of the findings presented in this paper, key results for an isolated cylinder at Re = 200 and two cylinder flows are reviewed.

3.1. ISOLATED CYLINDER, Re = 200

The flow solution for an isolated cylinder at Re = 200 was computed using the cell boundary element method, and a systematic study performed to quantify the effects of discretization parameters and convergence of solution as measured by the Strouhal frequency S (equal to fD/U, where f is the shedding frequency, U the free-stream velocity, and D the cylinder diameter), the drag coefficient C_D and lift coefficient C_L, derived from the proposed numerical scheme of study. Each computation was run until vortex shedding was established. When the shedding frequency changed by less than 0.5% per cycle (this was an arbitrary limit), the computation was assumed to have reached a periodic state.

For the computational domain size investigation as defined by front, back and side boundaries relative to the cylinder, it was found that the lift was most sensitive to the overall rectangular dimensions of the mesh domain, while the shedding frequency was quite robust. Furthermore, perhaps because of the periodic wake, the upstream boundary had slightly

TABLE 1

The effect of mesh refinement on the shedding frequency S, drag coefficient C_D and lift coefficient C_L for an isolated cylinder at Re = 200

Number of collocation points	S	C_D (time-averaged)	C_L (peak-to-peak)
2907	0·193	1·47	1·51
6037	0·193	1·39	1·50
8033	0·196	1·36	1·42
11358	0·196	1·36	1·42
15295	0·196	1·37	1·45

TABLE 2

The convergence in time of key vortex-shedding parameters for an isolated cylinder at Re = 200

Δt	S	C_D (time-averaged)	C_L (peak-to-peak)
0·2	0·203	1·39	1·46
0·1	0·196	1·36	1·42
0·05	0·196	1·36	1·40
0·025	0·196	1·36	1·43

more effect than the one downstream. From this global study it was concluded that boundaries positioned at $16D$ front, $14D$ back and $10D$ at the sides provide a good compromise between accuracy of solution and computational costs. (The $14D$ back is a suggested minimum value but this can be extended as desired.) These values corroborate the guideline values developed by Tezduyar & Shih (1991) and Behr et al. (1995) from different mathematical models and numerical schemes of study.

Mesh refinement checks were performed using five meshes (Farrant et al. 1999). The effect on vortex shedding is shown in Table 1. From these data it was decided to use the 8033 collocation point mesh with boundary conditions $(v_1 = 1, v_2 = 0)$ front, $(v_1 = 1, R_2 = 0)$ back and $(v_1 = 1, R_2 = 0)$ sides for further computations. Table 2 illustrates the influence of changing time step size and it was concluded that, as long as this key parameter was at least as small as $0·1$, the solution changed less than a few percent for all values. This study revealed that there was a small difference between the time-averaged drag value (calculated by integrating over the time period) and the mean of the peak and trough values on the drag curve. This difference was caused by numerical errors and found to disappear with decreasing time step. When $\Delta t = 0·1$, the error in the time-averaged drag value associated with this difference is less than 1%. For the computations presented in this paper a time step of $\Delta t = 0·1$ was chosen based on the considerations of both numerical accuracy and computational costs.

Because of the three-dimensional instabilities encountered in experiments (Williamson 1996), no experimental data are available for this two-dimensional vortex-shedding flow at Re = 200. However, a comparison with different numerical methods adopted by some other investigators for this problem was carried out (Farrant et al. 1999) and the results can be found in Table 3. There is a fairly good agreement between the results in this table, with the exception of the values obtained by Li et al. (1991).

TABLE 3

Values of Strouhal number, lift and drag coefficients for an isolated cylinder at Re = 200 determined by different methods

Investigator	Method	S	C_D (time-averaged)	C_L (peak-to-peak)
Braza et al. (1986)	Finite volume	0·2	1·32	1·55
Henderson (1995)	Spectral element	—	1·341	—
Li et al. (1991)	Finite element	0·18/0·187[‡]	1·17/1·04[†]	1·0/1·12[‡]
Slaouti & Stansby (1992)	Discrete vortex	0·196	—	1·25
Williamson & Brown[‡] (1998)	Spectral element	0·197	—	—
Zhang & Zhang (1997)	Finite volume	0·197	—	—
Present work	Cell BEM	0·196	1·36	1·42

[†] Depending on outflow boundary conditions.
[‡] Curve fit from data provided by R.D. Henderson.

This evidence clearly illustrates the influence of discretization and convergence of solution in the computation of key parameters. It was achieved by adopting an unstructured fluid mesh and, because optimization of the procedures in the numerical scheme of the study has not been performed, little is gained by undertaking extensive comparisons with other numerical methods relating to computer architectures, CPU times, etc. The aim of this part of the investigation was to demonstrate accuracy and convergence within the adopted methodology, to develop guidelines for the discretization of the fluid domain when multi-cylinder configurations are considered and to show limited comparisons with data determined by alternative numerical approaches (i.e. Table 3). For example, when examining the fluid–structure interactions between multiple-cylinder configurations, the overall domain size defined by front, back and side boundaries relates to the maximum domain constructed treating each cylinder as an isolated bluff body as previously discussed.

In a limited comparison with other methods, the computational cost, in CPU time, for the present method to solve the flow around an isolated cylinder at Re = 100 was measured. In this trial involving a fully developed steady-state solution before shedding occurred (Farrant et al. 1999), one shedding cycle was computed to an accuracy of 1% on the Strouhal shedding frequency (the correct value is taken as 0·164 for this Reynolds number) using 17 336 collocation points (two degrees of freedom per collocation point) and a time step size of 0·1 (the second-order time-stepping scheme was used). The CPU time for one shedding cycle was 5595 s on a Silicon Graphics Indigo 2, 195 MHz MIPS R10000 processor with 128MB RAM.

For finite difference and finite volume methods, the use of iterative procedures has been standard for some time. For incompressible flows, the pressure-correction-type algorithms are often used, particularly for structured meshes where the cost of matrix solution is usually low (Versteeg & Malalasekera 1995). For the cell BEM, the situation is more complicated because of the use of an unstructured mesh. However, the cell BEM has considerable similarity in its matrix structure with the finite element method. Therefore, some of the schemes developed for solving fluid problems with finite element methods provide a guide in the development of a scheme for the cell BEM. An example of the use of such iterative procedures can be found in Tezduyar et al. (1992).

3.2. FLOWS AROUND TWO CYLINDERS

For all arrangements of two cylinders, the separation of the cylinder surfaces is denoted by the nondimensional quantity g^* defined as

$$g^* = G/D, \tag{14}$$

where G is the minimum distance between the cylinder surfaces, and D is the cylinder diameter. This notation is adopted for the flows around arrays of cylinder configurations with Reynolds number defined on the basis of a single-cylinder diameter.

3.2.1. Cylinders in tandem, Re = 200

It is known from experiment [see, for example, Zdravkovich (1977)] that, when the cylinder spacing is approximately $g^* > 3.8$, the upstream cylinder in the tandem arrangement sheds in synchronization with the downstream one. To visualize the flow pattern in this regime, a particle simulation, for two cylinders in tandem at Re = 200 and $g^* = 4.0$ is shown in Figure 3 (Farrant et al. 1999). The particle simulation is generated from the velocity field of the cell boundary element method and indicates that shedding occurs from both cylinders. The time-averaged force coefficients and their deviations from the mean are shown for both cylinders in Table 4. The Strouhal frequency data confirm that the shedding is synchronized, in agreement with the experiment.

3.2.2. Cylinders side by side

The flow interaction between two cylinders side-by-side has been studied extensively by experimental investigations undertaken, for example, by Bearman & Wadcock (1973) and Williamson (1985). In particular, it is known that beyond a spacing of $g^* = 1.0$, shedding can occur in two possible synchronized modes, either in-phase or anti-phase (with respect to the variation of the lift coefficient). The vortex patterns associated with each of these modes are illustrated in Figure 4. For low Reynolds number laminar flows, Williamson (1985) found that each mode remained stable for many cycles, although the flow was capable of changing modes at any time due to perturbations arising during the experiment. With the cell BEM it was found (Farrant et al. 1999) that for spacings of approximately $g^* > 1.5$, it was possible for either mode to be computed for large numbers of shedding cycles (greater than 20, say). Validation was achieved for these geometries by making detailed comparisons with the streak-line photographs taken by Williamson (1985).

4. ARRAYS OF CYLINDERS OF VARIOUS TYPES AND ARRANGEMENTS

4.1. FLOWS AROUND FOUR CYLINDERS AT EQUAL SPACING

Flows around four equispaced cylinders of equal diameter were computed for two spacings and two flow alignments, see Figure 5. The two spacings considered were $g^* = 2.0$ and 4.0. For such layouts there are two extremes of flow alignment corresponding to a rotation of the entire arrangement by $45°$. For convenience, the configuration with two cylinders leading and two following, side-by-side, is considered to be the zero rotation case, the other, the $45°$ rotation case. All computations were performed at a Reynolds number of 200, based on one cylinder diameter.

For each of the four arrangements, the solution was computed until a periodic variation in the forces on the bodies was achieved. For most cases, periodicity was obtained after several thousand time steps at $\Delta t = 0.1$. Evaluation of the change in shedding frequencies,
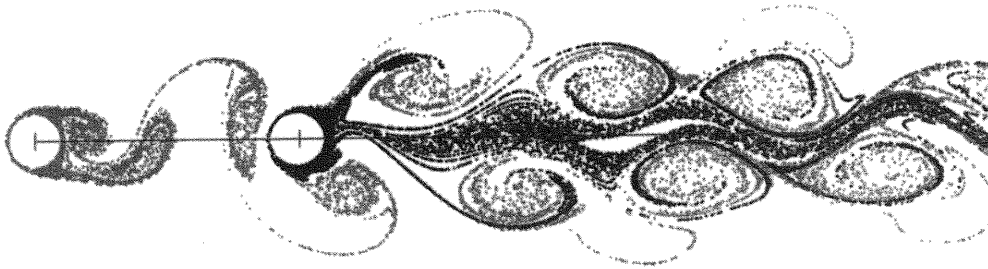
Figure 3. A particle simulation of the flow field around two cylinders in tandem at Re = 200 (based on one cylinder diameter) and $g^* = 4.0$.

TABLE 4

The shedding frequency S, drag coefficient C_D and lift coefficient C_L for cylinders in tandem at $g^* = 4.0$, Re = 200

Cylinder	S	C_D	$-$ ve	$+$ ve	C_L	$-$ ve	$+$ ve
Upstream	0·179	1·25	$-$ 0·05	0·07	0·00	$-$ 0·71	0·71
Downstream	0·179	0·38	$-$ 0·18	0·23	$-$ 0·00	$-$ 1·59	1·59
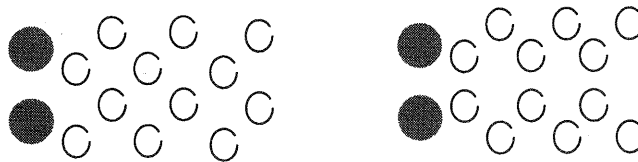
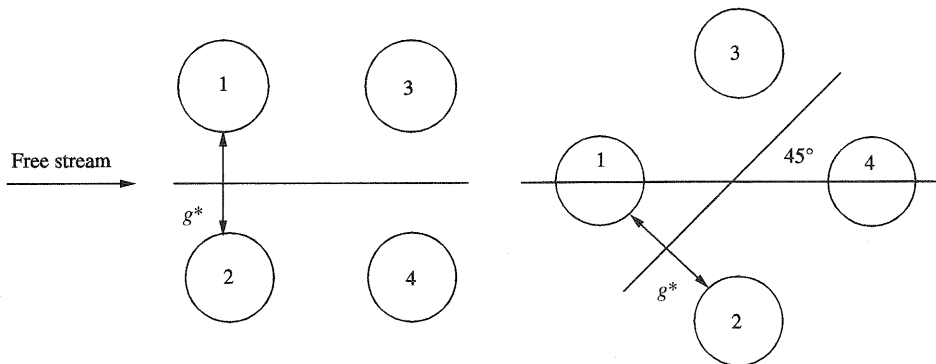Figure 4. In-phase (left) and anti-phase (right) shedding modes.

Figure 5. The two alignments of flow examined for four equispaced cylinders of equal diameter.

from cycle to cycle, was used as a measure of periodicity. The time step size was chosen to be $\Delta t = 0.1$, as previous validation suggested this would be sufficiently small. The extent and refinement of the mesh was also chosen according to the levels established by Farrant *et al.* (1999).

The results of the computations are presented in the following order: (i) $g^* = 2\cdot0$, no rotation; (ii) $g^* = 4\cdot0$, no rotation; (iii) $g^* = 2\cdot0$, rotation through $45°$; (iv) $g^* = 4\cdot0$, rotation through $45°$.

Values are given for the time-averaged lift and drag coefficients for each cylinder in every case. However, unlike the simple isolated cylinder case, the time-averaged value is no longer equivalent to the average of the peak values. This is because the vortex shed in the first part of one half cycle may no longer be of the same strength as that shed in the second, due to the presence of the other cylinders. Instead of quoting an amplitude plus or minus from the time-average, the maximum positive and negative deviations from the time-average are given separately. The greater the difference between these two maxima, the greater is the degree of interaction from surrounding cylinders. Although, for the reasons discussed in Section 3.1, at a time step size of $\Delta t = 0\cdot1$ a slight numerical error in the drag coefficient exists.

To provide insight into the behaviour of the flow field, particle simulations were used. This was done by introducing particles close to the surface of the cylinders and then convecting each in turn using the product of the velocity at the current location of the particle with the time-step size. Each particle was shaded according to the cylinder surface it originated from.

4.1.1. An alignment angle of $0°$

When the angle of rotation is zero and the spacing is small, $g^* = 2\cdot0$, the flow takes a considerable time to achieve a periodic and stable state. It was found that, the computation had to be continued to 6000 time steps or more in order to eliminate any long-lasting transient behaviour. This, perhaps, implies that the final solution is not very stable. In this respect, there were similarities with the flow around two cylinders side-by-side, where it is known that there is more than one shedding mode as discussed previously.

The eventual solution resulted in all cylinders shedding periodically, with identical frequencies, that is the shedding was synchronized. The frequencies and force coefficient values are listed in Table 5. A plot of three cycles for the lift and drag variation is shown in Figure 6, although the computation continued well beyond the region shown. Both the time-averaged values and the plots of the force coefficients reveal that there is a net repulsion between the cylinders across the flow. It is clear from the lift variation that the cylinders, alongside each other, are shedding in-phase. As with the case of two cylinders side-by-side, the vortices shed from between the cylinders are weaker and shed over a shorter period of time, compared to those on the outside. This means that, every other peak in the drag curve is subdued, creating a beat effect.

All the cylinders were affected by the presence of the others, and a common shedding frequency of $0\cdot177$ was established which is well below the isolated cylinder value of $0\cdot196$. Although the shedding frequencies were considerably changed, time-averaged drag coefficients of the upstream cylinders increased only slightly, while the lift amplitudes increased by around 25% when compared with the isolated cylinder.

The shedding from the downstream cylinders is influenced very strongly by the upstream flow. Although the time-averaged drag coefficient was found to be low, the amplitudes of both the lift and drag were found to be many times larger than experienced by an isolated cylinder and those of the upstream cylinders. The effect of the suppressed shedding from the inside of the cylinders is very pronounced, as illustrated by the alternate peaks of the drag curve and the distorted shape of the lift curve in Figure 6.

The description of the forces acting on the bodies is confirmed by an examination of the flow field using a particle simulation. Figure 7 shows a typical flow visualization using this

TABLE 5

The shedding frequency S, time-averaged drag, C_D, and lift coefficient, C_L, on each cylinder for four equispaced cylinders at spacing $g^* = 2 \cdot 0$ and Reynolds number Re = 200. The angle of alignment is zero. The + ve and − ve columns indicate the maximum and minimum differences from the time-averaged force coefficients

Cylinder	S	C_D	− ve	+ ve	C_L	− ve	+ ve
1	0·177	1·40	− 0·09	0·12	0·07	− 0·86	0·90
2	0·177	1·41	− 0·10	0·11	− 0·07	− 0·90	0·86
3	0·177	0·92	− 0·56	0·87	0·08	− 1·74	1·92
4	0·177	0·92	− 0·56	0·88	− 0·08	− 1·93	1·74
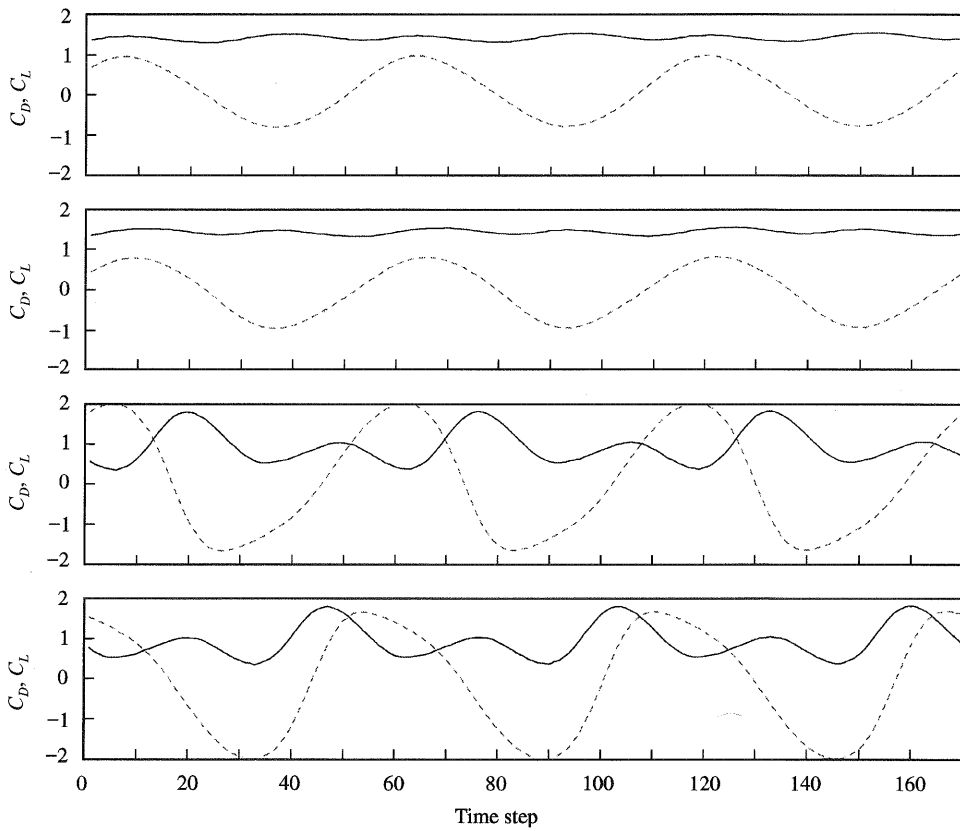
Figure 6. The coefficients of lift (C_L, broken lines) and drag (C_D, solid lines) on each cylinder for four equispaced cylinders at Re = 200 (based on one cylinder diameter) and $g^* = 2 \cdot 0$. The alignment to the flow is zero. The curves correspond to cylinders 1–4, top to bottom, respectively.

technique. Each graduation on the superimposed scale corresponds to a length of five diameters of a single cylinder. In this figure, synchronized, in-phase vortex shedding can be seen. Also, the synchronization of the shedding frequencies clearly arises due to the movement of the vortices shed from the upstream cylinders; these are indicated by the labels (a) and (b). The larger spread of the particles in vortex (a), as compared with (b),
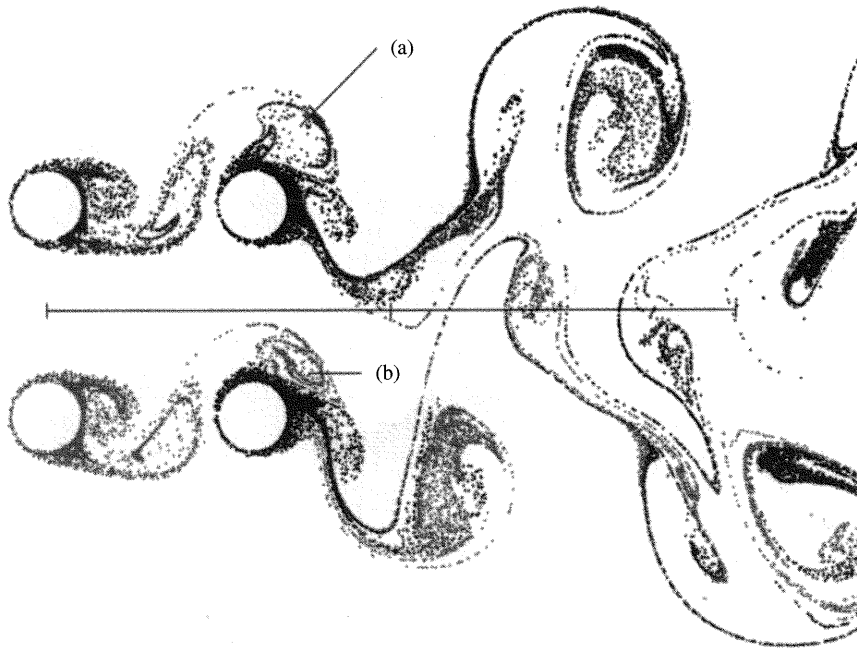
Figure 7. A particle simulation of the flow field around four equispaced cylinders at Re = 200 (based on one cylinder diameter) and $g^* = 2\cdot0$. The alignment to the flow is zero. The superimposed bar scale is 10 diameters long. In-phase shedding can clearly be seen. The vortices formed in between the cylinders are weaker than those on the outside. This is shown by the larger size vortex (a) compared with (b).

suggests that this vortex is stronger, which agrees with the larger forces found when shedding occurs from the outside of the cylinders.

When the spacing of the cylinders increases to $g^* = 4\cdot0$, keeping the angle of alignment at zero, Figure 8 shows that the interaction of the cylinders downstream remains strong although the cylinders upstream start to behave more like the isolated cylinder case. The calculated time averages and peak values of their force coefficients are listed in Table 6. Examination of these values for cylinders 1 and 2 (see Figure 5) indicates that the difference between these data and those for the isolated cylinder is less than 10%. Figure 8 demonstrates a weak interaction across the flow, because successive peaks in the drag curve are of a similar magnitude. This can be contrasted with the case where $g^* = 2\cdot0$ shown in Figure 6 in which every other peak is suppressed. For $g^* = 4\cdot0$, a weak repulsion exists between the upstream cylinders.

In spite of the similarity between the forces affecting the upstream cylinders with that of an isolated cylinder, the downstream cylinders show considerable interaction. This is due to the wake from the upstream cylinders, because the time-averaged lift values for the downstream cylinders are very nearly zero. The lift coefficient peaks are also of a similar size, indicating little interaction across the flow. It is interesting to note, however, that the downstream cylinders experience a very weak 'attractive' time-averaged force.

As with the previous case, the shedding from all cylinders is synchronized, but the frequency is higher and closer to the isolated cylinder value. This is probably a result of the upstream cylinders controlling the shedding on those further downstream. A similar behaviour was found for the tandem arrangement in Section 3.2.1. At this spacing of

TABLE 6

The shedding frequency S, time-averaged drag, C_D, and lift coefficient, C_L, on each cylinder for four equispaced cylinders at spacing $g^* = 4{\cdot}0$ and Reynolds number Re = 200. The angle of alignment is zero

Cylinder	S	C_D	$-$ ve	$+$ ve	C_L	$-$ ve	$+$ ve
1	0·190	1·37	$-$ 0·06	0·09	0·05	$-$ 0·75	0·74
2	0·190	1·37	$-$ 0·06	0·09	$-$ 0·05	$-$ 0·74	0·75
3	0·190	0·67	$-$ 0·25	0·40	$-$ 0·02	$-$ 1·92	2·00
4	0·190	0·66	$-$ 0·24	0·40	0·02	$-$ 2·00	1·91
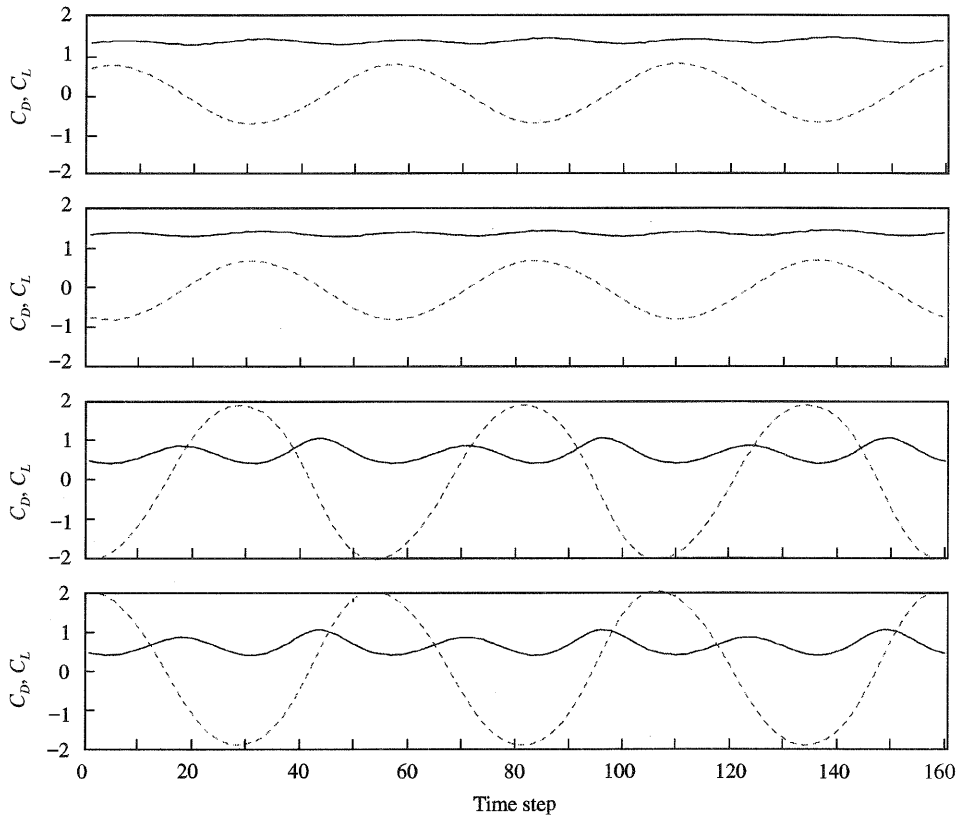
Figure 8. The coefficients of lift (C_L, broken lines) and drag (C_D, solid lines) on each cylinder for four equispaced cylinders at Re = 200 (based on one cylinder diameter) and $g^* = 4{\cdot}0$. The alignment to the flow is zero. The curves correspond to cylinders 1–4, top to bottom, respectively.

$g^* = 4{\cdot}0$, an anti-phase mode of shedding occurs and appears to be a stable solution. The symmetry in the flow field is clearly seen in the particle simulation illustrated in Figure 9.

4.1.2. *An alignment angle of* 45°

When the arrangement of the four cylinders is rotated by 45°, the resulting behaviour of the flow becomes less intuitive due to the increased difficulty of synchronized vortex shedding
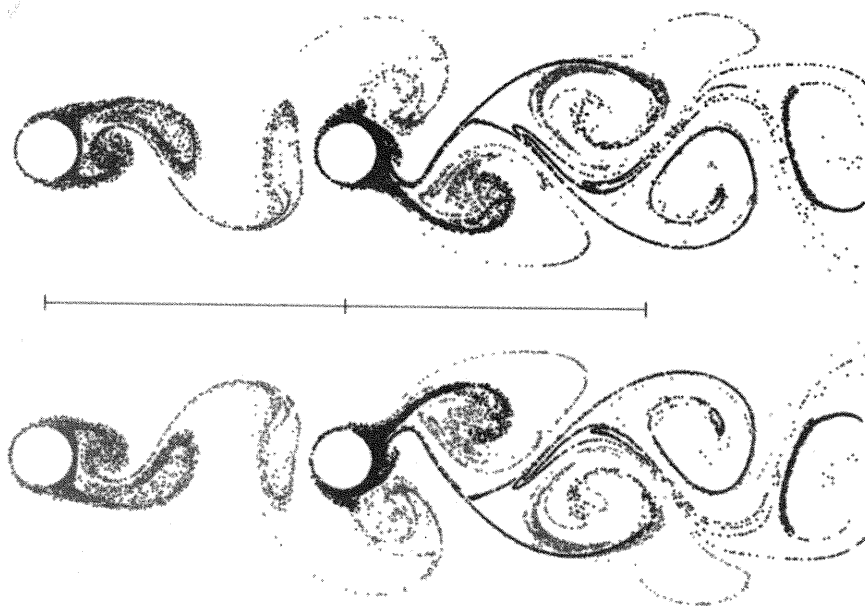
Figure 9. A particle simulation of the flow field around four equispaced cylinders at Re = 200 (based on one cylinder diameter) and $g^* = 4\cdot0$. The alignment to the flow is zero. The superimposed bar scale is 10 diameters long. Anti-phase shedding can be seen.

from all cylinders When the interaction is strongest, at $g^* = 2\cdot0$, the flow does not reach a periodic state in each lift oscillation but, instead, repeats in every other. This behaviour is most marked on the cylinder furthest downstream (i.e. cylinder 4 in Figure 5) as demonstrated in Figure 10 by the variation of the lift coefficient with time. The four different peak values, (1)–(4), illustrate the repeat sequence within the extended period.

For cylinder 4 the drag force oscillates at twice the rate of the lift force corresponding to the situation for an isolated cylinder. However, the middle cylinders 2 and 3 show drag characteristics oscillating at the same rate as the lift components. Furthermore, Figure 10 shows that the shedding from cylinders 2 and 3 is not exactly the same, as demonstrated by the variation of the drag with time for each cylinder. This behaviour also manifests itself in the time-averaged values and maximum positive and negative deviations of the lift and drag coefficients in Table 7. Similarity exists in the magnitudes for cylinders 2 and 3, but they are not identical. On average, there is a slight repulsive force between cylinders 2 and 3. Cylinder 4 experiences a non-zero average lift force, in spite of lying on the centre line of the arrangement.

The leading cylinder 1 does not experience strong shedding, and the forces on the cylinder repeat every oscillation of the lift. A comparison of the force magnitudes with those on an isolated cylinder confirms that the strength of the shedding is subdued and at a higher frequency (8%). This is presumably due to the presence, in particular, of the middle cylinders 2 and 3, which restrict the rolling up of the separated shear layers.

Particle simulation fields were calculated for each peak in the lift through one period of repetition, that is at the times denoted by (1)–(4) in Figure 10. The respective flow simulations are shown in Figures 11 and 12. It can be seen that, although the shedding from the upstream cylinders looks very similar at times (1) and (3), and likewise (2) and (4), the wake area is very different. Clearly, the wake structure is very sensitive to the strength and timing of the vortex shedding from each cylinder.
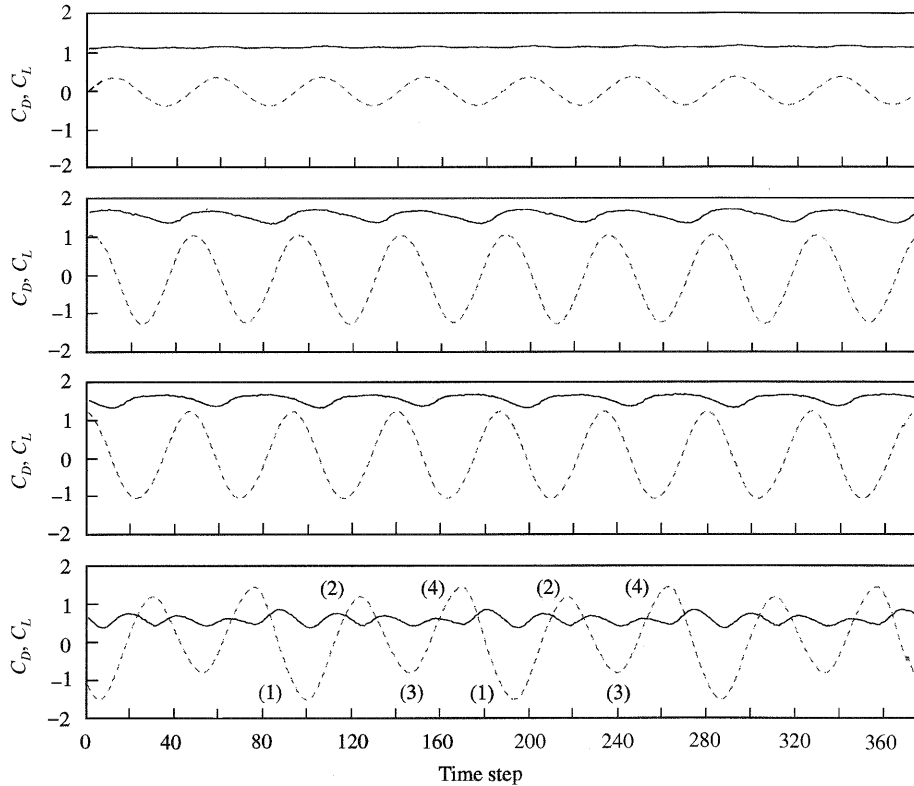
Figure 10. The coefficients of lift (C_L, broken lines) and drag (C_D, solid lines) on each cylinder for four equispaced cylinders at Re = 200 (based on one cylinder diameter) and $g^* = 2\cdot0$. The flow is aligned at 45°. The curves correspond to cylinders 1–4, top to bottom, respectively. The numbers (1)–(4) indicate the sequence of peaks in the lift through one period of repetition.

TABLE 7

The variation of the drag and lift on four equispaced cylinders at a separation of $g^* = 2\cdot0$, aligned at 45° to the flow and Re = 200. C_D and C_L are the time-averaged drag and lift coefficients, respectively, while T is the time period for repetition of the shedding. For cylinders 2–4 the forces repeat after two oscillations of the lift. On the first cylinder, the forces repeat every oscillation of the lift. The columns marked $+$ve and $-$ve denote the maximum and minimum differences from the time averaged values

Cylinder	T^{-1}	C_D	$-$ve	$+$ve	C_L	$-$ve	$+$ve
1	0·107	1·14	$-$0·01	0·04	0·00	$-$0·37	0·37
2	0·107	1·53	$-$0·20	0·19	$-$0·07	$-$1·21	1·12
3	0·107	1·55	$-$0·21	0·14	0·08	$-$1·11	1·17
4	0·107	0·58	$-$0·20	0·28	0·07	$-$1·58	1·53

Moving the cylinders further apart, to a spacing of $g^* = 4\cdot0$, but keeping the alignment of the flow at 45°, dramatically reduces the interaction between all the cylinders, except cylinder 4, which is directly in the wake of cylinder 1. As a result of the weak interaction, the force coefficients for cylinders 1–3 are all very close to those found for an isolated cylinder,
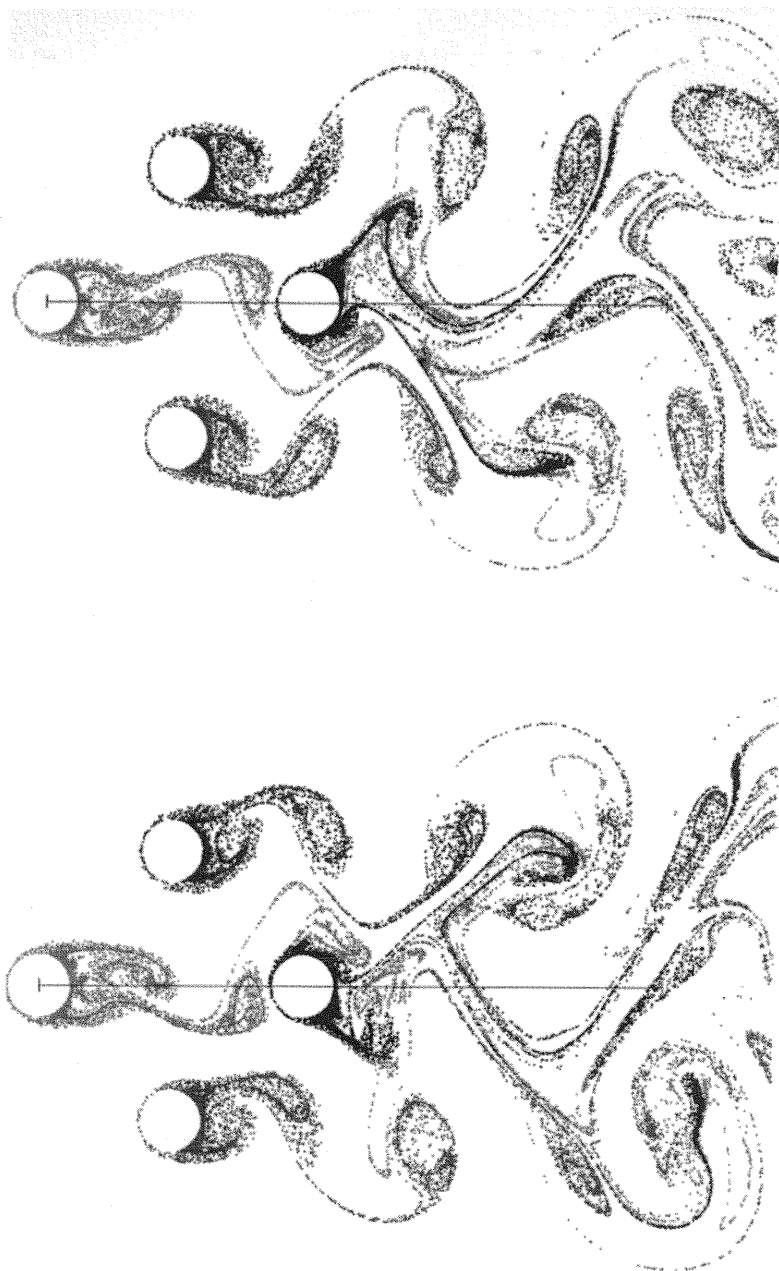
Figure 11. A particle simulation of the flow around four equispaced cylinders at spacing $g^* = 2\cdot0$ and Re = 200. The alignment angle to the flow is 45°. The top picture is at time (1), when the lift on the last cylinder is at a negative peak. The bottom picture is at time (2), when the lift on the last cylinder is at a positive peak, see Figure 10. The superimposed bar scale is 10 diameters long.
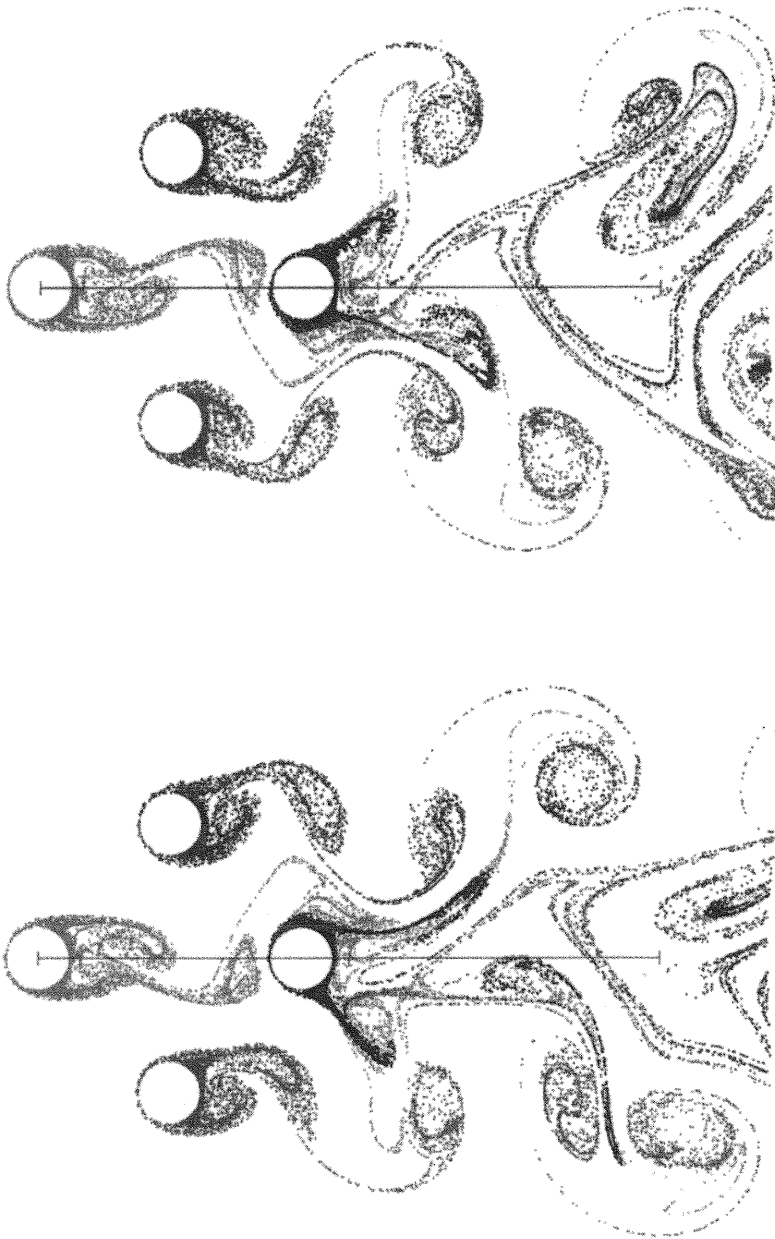
Figure 12. A particle simulation of the flow around four equispaced cylinders at spacing $g^* = 2 \cdot 0$ and Re $= 200$. The alignment angle to the flow is $45°$. The top picture is at time (3), when the lift on the last cylinder is at a negative peak. The bottom picture is at time (4), when the lift on the last cylinder is at a positive peak, see Figure 10. The superimposed bar scale is 10 diameters long.

TABLE 8

The shedding frequency S, time-averaged drag, C_D, and lift coefficient, C_L, on
each cylinder for four equispaced cylinders at spacing $g^* = 4.0$ and Reynolds
number Re $= 200$. The angle of alignment is $45°$

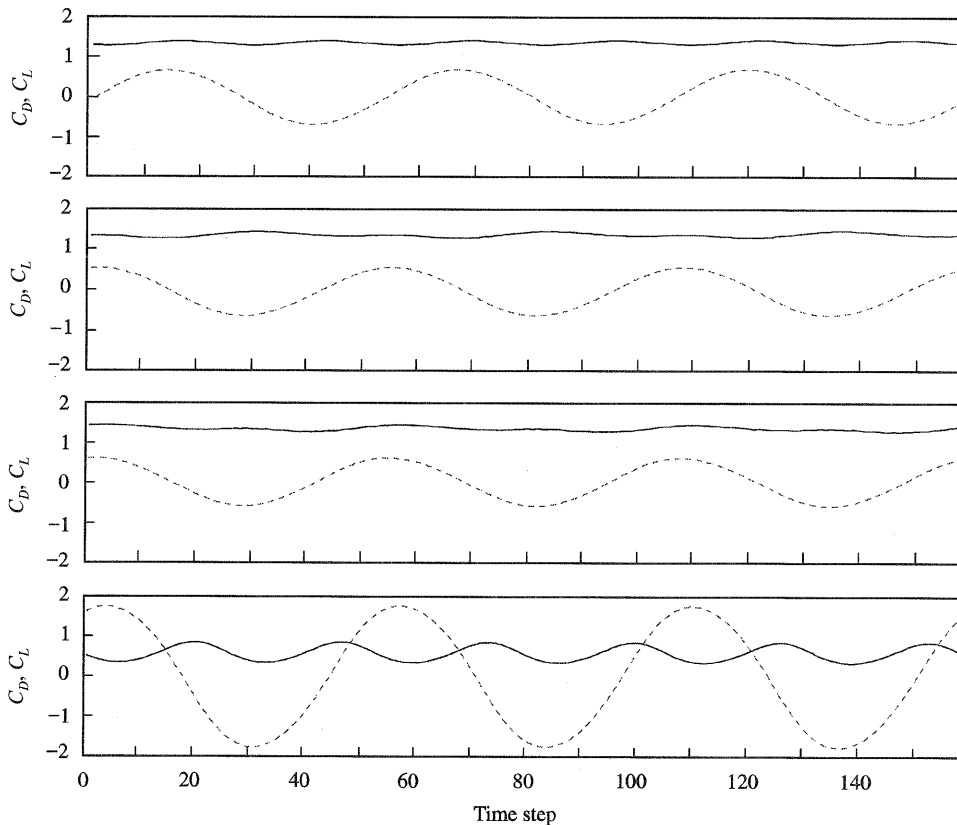| Cylinder	S	C_D	$-$ ve	$+$ ve	C_L	$-$ ve	$+$ ve
1	0.189	1.33	-0.04	0.06	0.00	-0.68	0.68
2	0.189	1.36	-0.07	0.10	-0.04	-0.60	0.60
3	0.189	1.36	-0.07	0.10	-0.04	-0.60	0.60
4	0.189	0.59	-0.24	0.28	0.0	-1.76	1.76

Figure 13. The coefficients of lift (C_L, broken lines) and drag (C_L, solid lines) on each cylinder for four equispaced cylinders at Re $= 200$ (based on one cylinder diameter) and $g^* = 4.0$. The arrangement is aligned at $45°$ to the flow. The curves correspond to cylinders 1–4, top to bottom, respectively.

see Table 8, although there is a weak repulsion between cylinders 2 and 3. The interaction between cylinders 2 and 3 results in a slight suppression of alternate peaks in the variation of the drag curves for these cylinders, as shown in the plots in Figure 13. Cylinder 4 experiences a much greater lift force than all the other cylinders. This is of zero mean value which is to be expected given the very weak interaction of cylinders 2 and 3. A comparison of particle simulation for the arrangement of four cylinders in the wake area of cylinder 4 (Figure 14) shows considerable similarity with the wake area behind
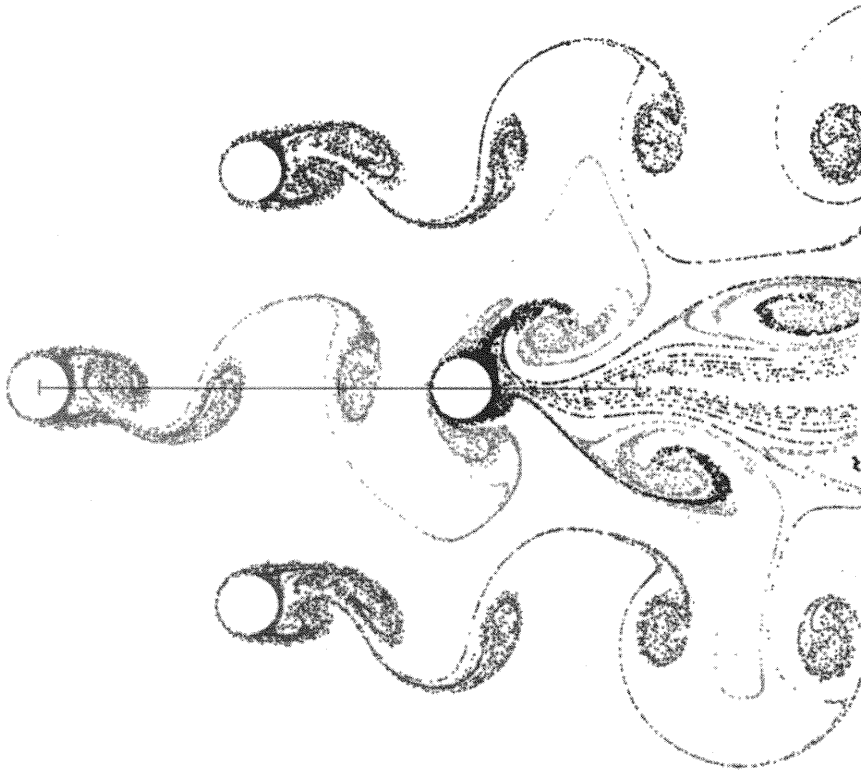
Figure 14. A particle simulation of the flow field around four equispaced cylinders at Re = 200 (based on one cylinder diameter) and $g^* = 4.0$. The arrangement is aligned at 45° to the flow. The superimposed bar scale is 10 diameters long. In-phase shedding can be seen at the middle cylinders.

the tandem arrangement illustrated in Figure 3. The only visible differences arise from the outermost streaks which are swept up and incorporated into the vortex streets of cylinders 2 and 3.

4.2. Flows Around an Elliptical and a Circular Cylinder

Results are presented for the two-dimensional flow around an elliptical cylinder in close proximity to a circular cylinder. Figure 15 illustrates the bluff-body configurations examined. As can be seen, the across-flow orientation can be transformed into the in-line case by a simple rotation of 90°. The ratio of the minor axis dimension of the elliptical cylinder or the diameter of the circular cylinder to the elliptical cylinder major axis is $1/\sqrt{2}$.

According to Massey (1989), the characteristic length for the definition of Reynolds number relates to the largest bluff body dimension across the flow. Thus, if the geometry transformation between the two cases under consideration is just a rotation through 90°, then the Reynolds numbers in the two cases will be different. That is, the Reynolds number of the in-line configuration, Re_i, is related to that of the across-flow configuration, Re_a, by $Re_a = \sqrt{2}Re_i$. Using this definition of Reynolds number, a computation was carried out with the geometry in the across-flow orientation at Reynolds number $Re_a = 200$. Therefore,
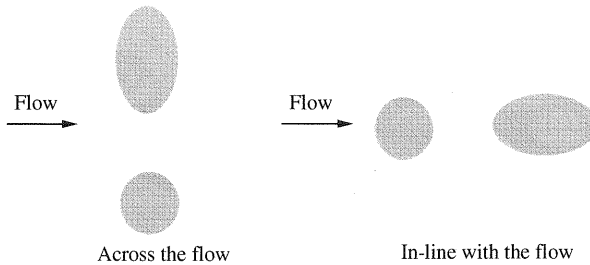
Figure 15. The two alignments of the elliptical and circular cylinder to the flow. One arrangement is transformed to the other by a clockwise rotation through 90°.

the Reynolds number for the computation with the geometry in-line with the flow was approximately $Re_i = 141$. This is simply confirmation of the effect of rotating the geometry which leads to a smaller body section across the flow for the in-line case.

The force coefficients, C_D and C_L, were calculated using the dimension, across the flow, of the corresponding body. This is also true for the Strouhal frequency which can be redefined as

$$S = \frac{fL}{U},$$

where f is the shedding frequency, U the free-stream velocity, and L the characteristic length of the body (i.e. the length of the ellipse in the across-flow configuration and the cylinder diameter in the in-line arrangement).

These definitions of characteristic length allow a measure of comparison of the results with those of similarly shaped isolated bodies. Comparison of the nondimensional parameters between the two orientations of geometry is not directly possible.

The nondimensional gap parameter was set in both orientations to be $g^* = 3\cdot0$, nondimensionalized against the major axis dimension of the elliptical cylinder. That is,

$$g^* = \frac{G}{L_e}.$$

Here G is the minimum gap between the surfaces of the bodies, and L_e is the length of the ellipse. For convenience, the definition of g^* remains unchanged with the orientation of the bluff bodies to the flow.

4.2.1. In-line with the flow

When the elliptical cylinder is directly in the wake of the upstream cylinder at a separation of $g^* = 3\cdot0$ and $Re = 141$, vortex shedding into the wake is synchronized. The flow around the cylinders is very similar to that found when the two bodies are circular cylinders. This is evident from a comparison of the particle simulations shown in Figures 16 and 3. When the average and peak values of the lift coefficient C_L and drag coefficient C_D (see Table 9) are compared with those calculated for two circular cylinders in Section 3.2.1 (at a different Reynolds number and spacing) it is again found that there exists much similarity. The upstream circular cylinder sheds a vortex flow onto the elliptical cylinder, thus increasing the strength of the vortex shedding on this cylinder considerably. The time-averaged lift values are zero in all cases, and the drag on the downstream elliptical cylinder is greatly reduced.
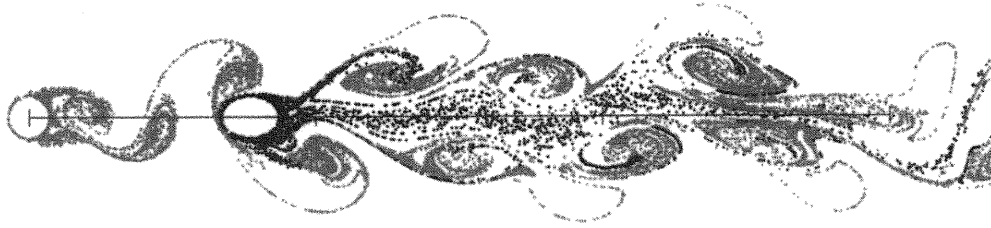
Figure 16. A particle simulation of the flow field around an elliptical cylinder downstream of a circular cylinder at Re = 141 (based on the circular cylinder diameter) and $g^* = 3\cdot0$ (based on the largest dimension of the elliptical cylinder). The superimposed bar scale is 15 times the length of the largest dimension of the elliptical cylinder.

TABLE 9

The shedding frequency f, Strouhal shedding frequency S, drag coefficient C_D and lift coefficient C_L for a circular cylinder in line and in front of elliptical cylinder. The Reynolds number, Re = 141, is based on the largest body dimension across the flow. The spacing $g^* = 3\cdot0$, based on the largest dimension of the elliptical cylinder. The Strouhal shedding frequency was calculated for an isolated circular cylinder at Re = 141 from the empirical formula provided by Williamson (1991)

Cylinder	f	S	C_D	− ve	+ ve	C_L	− ve	+ ve
Circular	0·234	0·166	1·22	− 0·02	0·04	0·00	− 0·50	0·50
Elliptical	0·234	0·166	0·42	− 0·18	0·21	0·00	− 1·77	1·77
Williamson (1991)	—	0·181	—	—	—	—	—	—

Alongside the force data for the in-line circular and elliptical cylinder case presented in Table 9 is the shedding frequency for an isolated cylinder at Re = 141. This shedding frequency was calculated from the empirical formula provided by Williamson (1991). From these data it is seen that the close proximity of the two cylinders acts to reduce the shedding frequency. A similar result was also computed for the case of the two circular cylinders in tandem (see Section 3.2.1).

4.2.2. Across the flow

When the arrangement of the elliptical and circular cylinder is rotated through 90°, so that it is across the flow, the Reynolds number is raised due to the increased cross-section of the elliptical cylinder which is presented to the flow. In this case, the computation was carried out at a Reynolds number of Re = 200. The separation remained unchanged at $g^* = 3\cdot0$, based on the major axis dimension of the elliptical cylinder.

The computed solution revealed that the circular cylinder shed vortices at a different frequency to the elliptical cylinder. This was expected, because of the different cross-sectional dimensions presented to the oncoming flow. The interaction of the two cylinders generates an *amplitude modulation* or *beat*-type phenomenon as displayed in Figure 17 in the variation of the lift and drag coefficients of both cylinders. Although the modulation effect is present in the force variation for both cylinders, it is most noticeable for the circular cylinder because of weaker shedding. As computational time proceeded, the shedding from the two bluff bodies constantly shifted from in- to anti-phase (see Figure 18). When the shedding is in-phase the amplitudes of the lift and drag forces on both bodies are at their maxima. Conversely, when the shedding is in anti-phase the amplitudes of the lift and drag forces are at their minima.
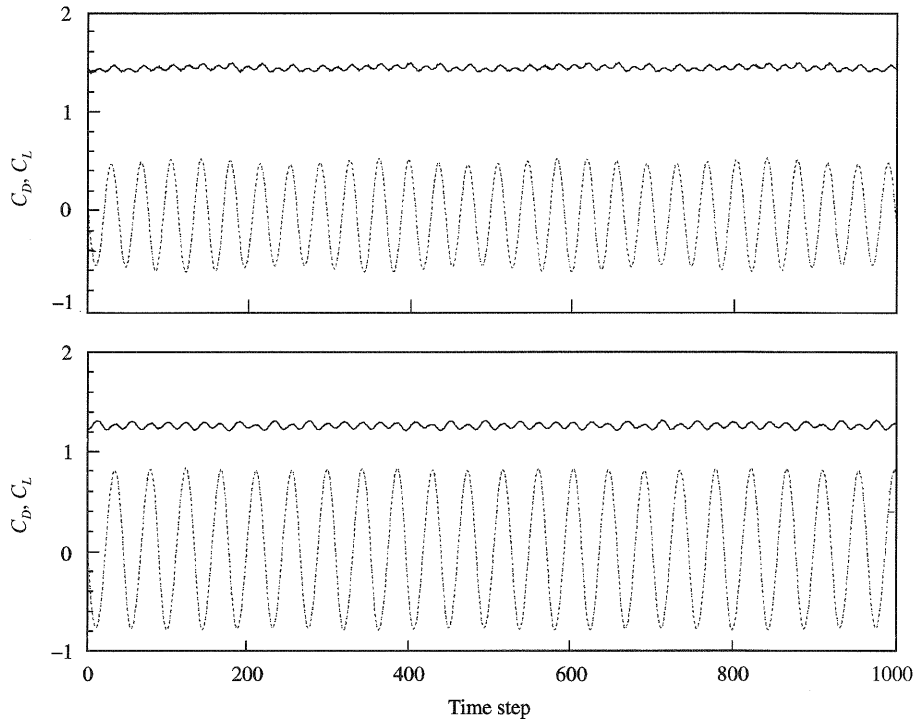
Figure 17. The variation of the lift coefficient C_L (broken line) and the drag coefficient C_D (solid line) for a circular cylinder (top curves) and an elliptical cylinder (bottom curves) arranged across the flow. The *amplitude modulation* effect is seen and is due to the different shedding frequencies of each body. The Reynolds number for the computation is Re = 200 and spacing is $g^* = 3.0$, both based on the largest dimension of the elliptical cylinder.
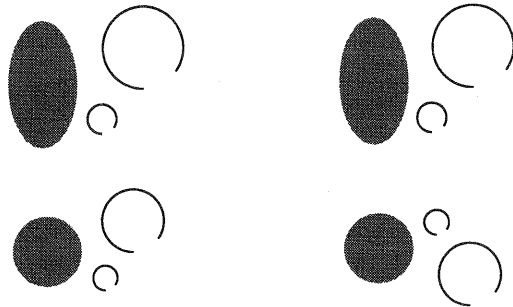

Figure 18. In-phase (left) and anti-phase (right) vortex-shedding modes from a circular and elliptical cylinder (shaded areas) arranged across the flow.

Although the shedding phases change, their frequencies remain constant. For the elliptical cylinder a Strouhal shedding frequency of 0·229 was determined, exceeding the value of 0·196 computed in Section 3.1 for an isolated circular cylinder at the same Reynolds number. The circular cylinder sheds at a Strouhal frequency of 0·192, which is higher than the Strouhal frequency of 0·181 calculated from the empirical formula provided by Williamson (1991). For the calculation using the empirical formula, an effective Reynolds number of Re = 141 was taken rather than the Reynolds number for the whole computation which was at Re = 200.
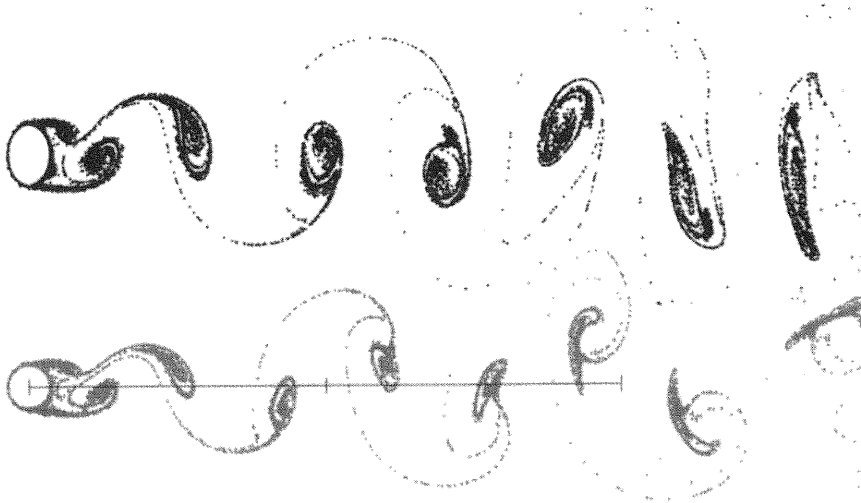
Figure 19. A particle simulation of the flow field around a circular and elliptical cylinder at Re = 200 and $g^* = 3\cdot0$ both based on the largest dimension of the elliptical cylinder. Each graduation on the superimposed bar scale is five times the largest dimension of the elliptical cylinder.

Figure 19 illustrates a typical in-phase particle simulation of the flow into the wake. The different wake patterns are clearly visible (i.e., 8 and 7 vortices behind the cylinder and ellipse, respectively), a degree of repetition and all the ingredients generating a beat-type phenomenon.

5. CONCLUSIONS

A cell boundary element method was used to investigate unsteady flow solutions to more complicated geometries than the standard cases of two circular cylinders in tandem or side-by-side as previously described by Farrant *et al.* (1999).

Flows around four equispaced circular cylinders of equal diameter were solved for two orientations and spacings, making four combinations in total. In the case when the cylinders were in two pairs across the stream, similar features were observed in the flow when compared with the tandem and side-by-side arrangements. That is, when the spacing was small ($g^* = 2\cdot0$), an in-phase vortex-shedding mode occurred. However, for increased cylinder spacing an anti-phase vortex-shedding mode dominated, with the wake pattern resembling the flow of two tandem pairs placed alongside each other. Given that both the in-phase and anti-phase modes were only achieved after a considerable computational time (suggesting that they are not very stable) the ability to cause switching from one mode to the other by applying a suitable perturbation was difficult to confirm. Such switching behaviour for the side-by-side arrangement was confirmed and observed in the previous study of Farrant *et al.* (1999).

When the arrangement is rotated through 45°, so that there is only one pair across the flow and one cylinder upstream and downstream, and the spacing is kept small ($g^* = 2.0$), the flow behaviour becomes more disordered. In fact, the shedding process was found to repeat in every other oscillation of the lift, and more disordered flow patterns were seen in the wake. At larger spacings ($g^* = 4\cdot0$), the outer cylinders shed synchronously and the shedding repeated in every lift cycle. This would suggest that, as with the side-by-side arrangement, the closer spacings result in disordered and aperiodic flow.

The flow around a circular cylinder and an elliptical cylinder in-line and across the flow revealed the effect of different characteristic body dimensions on the vortex shedding. When the circular cylinder was in-line and upstream of the elliptical cylinder it was found that shedding was synchronized, with a very strong interaction between the two bodies. When the two bluff bodies, with their different characteristic lengths, were placed across the flow, the interaction was weaker and the cylinders shed vortices at different frequencies. Consequently, the shedding from each cylinder constantly moved in- and out-of-phase, reinforcing and reducing the shedding strength in the process. This effect has similarity with *amplitude modulation* or *beat* phenomena.

In all these investigations the use of the cell boundary element method using an unstructured fluid domain mesh idealization proved straightforward and required no modification for variation of the number of bodies or their shape.

Reference

BARLTROP, N. D. P. & ADAMS, A. J. 1991. *Dynamics of Fixed Marine Structures.* Oxford: Butterworth Heinemann.

BATHE, K. -J. & WILSON, E. L. 1976. *Numerical Methods in Finite Element Analysis.* Englewood Cliffs, NJ: Prentice-Hall Inc.

BEARMAN, P. & WADCOCK, A. 1973. The interaction between a pair of cylinders normal to a stream. *Journal of Fluid Mechanics*, **61**, 499–511.

BEHR, M., HASTREITER, D., MITTAL, S. & TEZDUYAR, T. E. 1995. Incompressible flow past a circular cylinder: Dependence of the computed flow field on the location of the lateral boundaries. *Computer Methods in Applied Mechanics and Engineering*, **123**, 309–316.

BISHOP, R. & HASSAN, A. 1964. The lift and drag forces on a circular cylinder in a flowing fluid. *Proceedings of the Royal Society (London)* Series A, **277**, 51–75.

BLEVINS, R. D. 1990. *Flow-Induced Vibration.* New York: Van Nostrand Reinhold.

BRAZA, M., CHASSAING, P. & MINH, H. H. 1986. Numerical study and physical analysis of the pressure and velocity fields in the near wake of a circular cylinder. *Journal of Fluid Mechanics*, **165**, 79–130.

BREBBIA, C. A. 1978. *The Boundary Element Method for Engineers.* London: Pentech Press.

BREBBIA, C. A. & WALKER, S. 1980a. *Boundary Element Techniques in Engineering.* London: Newness-Butterworths.

BREBBIA, C. A. & WALKER, S. 1980b. Steady and unsteady potential problems using the boundary element method. In *Recent Advances in Numerical Methods in Fluids*, Volume 1, p. 1. Swansea, U.K.: Pineridge Press.

CHANG, K. & SONG, C. 1990. Interactive vortex shedding from a pair of circular cylinders in a transverse arrangement. *International Journal for Numerical Methods in Fluids* **11**, 317–329.

CHENG, L. & ARMFIELD, S. W. 1994. Large eddy simulation of wave and current induced flow over a circular cylinder. In *Proceedings BOSS 94*, pp. 655–664.

COOK, R. D., MALKUS, D. S. & PLESHA, M. E. 1989. *Concepts and Applications of Finite Element Analysis.* New York: John Wiley and Sons.

FARRANT, T. 1999. The boundary element method applied to viscous and vortex shedding flows around cylinders. Ph.D. Thesis, Department of Ship Science, Faculty of Engineering and Applied Science, University of Southampton.

FARRANT, T., TAN, M. & PRICE, W. G. 1999. A cell boundary element method applied to laminar vortex shedding from circular cylinders. *Computers and Fluids* (to be published).

GATSKI, T. B., YOUSUFF HUSSANI, M. & LUMLEY, J. 1996. *Simulation and Modeling of Turbulent Flows.* New York: Oxford University Press.

GRAN, S. 1992. *A Course in Ocean Engineering.* Amsterdam: Elsevier.

HASSAN, A. Y. 1962. The effect of vibration on the lift and drag forces on a circular cylinder in a fluid flow. Ph.D. Thesis, University College London, University of London.

HATTON, S. A. 1999. Update on the design of steel catenary riser systems. In *Deep and Ultra-Deep Water Offshore Technology.* Society of Underwater Technology, 25–26 March 1999, University of Newcastle, U.K.

HENDERSON, R. D. 1995. Details of the drag curve near the onset of vortex shedding. *Physics of Fluids* **7**, 2102–2104.

HUNT, J. C. R. 1995. Practical and fundamental developments in the computational modelling of fluid flows. *Proceedings of the Institution of Mechanical Engineers* **209**, 297–314.

JOHNSON, A. A., TEZDUYAR, T. & LIOU, J. 1993. Numerical simulation of flows past periodic arrays of cylinders. *Computational Mechanics* **11**, 371–383.

LI, J., CHAMBAREL, A., DONNEAUD, M. & MARTIN, R. 1991. Numerical study of laminar flow past one and two cylinders. *Computers and Fluids* **19**, 155–170.

MASSEY, B. S. 1989. *Mechanics of Fluids*, 6th edition. London: Chapman & Hall.

MITTAL, S., KUMAR, V. & RAGHUVANSHI, A. 1997. Unsteady incompressible flows past two cylinders in tandem and staggered arrangements. *International Journal For Numerical Methods in Fluids* **25**, 1315–1344.

PERSILLON, H., BRAZA, M. & JIN, G. 1995. Prediction of transition features in the flow past a circular cylinder in three-dimensions. In *Proceedings of the 5th International Offshore and Polar Engineering Conference*, Volume 3, pp. 597–602. The International Society of Offshore and Polar Engineers.

PRICE, W. G. & TAN, M. 1990. The calculation of fluid actions on manoeuvring arbitrary shaped submerged bodies using viscous boundary elements. In *Proceedings 18th Symposium on Naval Hydrodynamics*, pp. 804–814, Ann Arbor, MI., U.S. Office of Naval Research.

PRICE, W. G. & TAN, M. 1992. Applications of viscous boundary element method in hydrodynamic problems relating to manoeuvering bodies. In *Proceedings of 19th Symposium on Naval Hydrodynamics*, pp. 437–447, Seoul, Korea, U.S. Office of Naval Research.

SARPKAYA, T. & ISAACSON, M. 1981. *Mechanics of Wave Forces on Offshore Structures*. New York: Van Nostrand Reinhold.

SLAOUTI, A. & STANSBY, P. 1992. Flow around two circular cylinders by the random vortex method. *Journal of Fluids and Structures* **6**, 641–670.

SLAOUTI, A. & STANSBY, P. K. 1994. Force oscillation and dynamic response of a circular cylinder in a current-investigation by the vortex method. In *Proceedings BOSS 94*, pp. 645–654.

TAN, M. 1994. A viscous boundary element approach to fluid flow-structure interaction problems. Ph.D. Thesis, Department of Ship Science, Faculty of Engineering and Applied Science, University of Southampton.

TAN, M., FARRANT, T. & PRICE, W. G. 1999. A cell boundary element method for viscous laminar flow solutions. *Proceedings of the Royal Society (London) Series A*, **455**, 4277–4304.

TEZDUYAR, T. E., LIOU, J., GANJOO, K. & BEHR, M. 1990. Solution techniques for the vorticity-streamfunction formulation of two-dimensional unsteady incompresible flows. *International Journal for Numerical Methods in Fluids*, **11**, 515–539.

TEZDUYAR, T. E. & MITTAL, S. 1992. Finite element computation of incompressible flows. In *Computational Non-linear Mechanics in Aerospace Engineering*, Chapter 11, pp. 417–447.

TEZDUYAR, T. E. & SHIH, R. 1991. Numerical experiments on downstream boundary of flow past a cylinder. *Journal of Engineering Mechanics* **117**, 854–871.

TOSAKA, N. & KAKUDA, K. 1988. The generalised boundary element method for nonlinear problems. In *Boundary Elements X. Proceedings of the 10th International Conference Boundary Element Methods* (ed. C. Brebbia), Southampton: Computational Mechanics Publications.

VAN DE VOSSE, F., SEGAL, A., VAN STEENHOVEN, A. A. & JANSEEN, J. 1986. A finite element approximation of the unsteady two dimensional Navier–Stokes equations. *International Journal for Numerical Methods in Fluids* **6**, 427–443.

VERSTEEG, H. K. & MALALASEKERA, W. 1995. *An Introduction to Computational Fluid Dynamics.* Harlow, U.K.: Longman Group Limited.

WILLIAMSON, C. H. K. 1985. Evolution of a single wake behind a pair of bluff bodies. *Journal of Fluid Mechanics* **159**, 1–18.

WILLIAMSON, C. H. K. 1991. 2-D and 3-D aspects of the wake of a cylinder, and their relation to wake computations. *Lectures in Applied Mathematics* **28**, 719–751.

WILLIAMSON, C. H. K. 1996. Vortex dynamics in the cylinder wake. *Annual Review of Fluid Mechanics* **28**, 477–539.

WILLIAMSON, C. H. K. & BROWN, G. L. 1998. A series in $(1/\sqrt{Re})$ to represent the Strouhal–Reynolds number relationship of the cylinder wake. *Journal of Fluids and Structures* **13**, 1073–1085.

ZDRAVKOVICH, M. M. 1977. Review of flow interference between two circular cylinders in various arrangements. *ASME Journal of Fluids Engineering* **99**, 618–633.

ZHANG, H. & ZHANG, X. 1997. Flow structure analysis around an oscillating circular cylinder at low KC number : a numerical study. *Computers and Fluids* **26**, 83–106.